

# Gabor filter design for multiple texture segmentation

Thomas P. Weldon , William E. Higgins<sup>†</sup>, Dennis F. Dunn<sup>††</sup>

**Abstract**— A method is presented for the design of a single Gabor filter for the segmentation of multi-textured images. Earlier methods were limited to filters designed for one or two textures or were limited to filters selected from a predetermined filter bank. Our proposed method yields new insight into the design of Gabor filters for segmenting multi-textured images and lays an essential foundation for the design of multiple Gabor filters. In the method, Rician statistics of filtered textures at two different Gabor-filter envelope scales are used to efficiently generate probability density estimates for each filtered texture over an extensive set of candidate filter parameters. Variable degrees of postfiltering and the accompanying effect on postfilter output statistics are also included in the design procedure. The result is a unified framework that analytically relates the texture power spectra, Gabor-filter parameters, postfiltering effects, and image-segmentation error. Finally, the resulting filter design is based on all constituent textures and is not constrained to a limited set of candidate filters.

**Keywords**— Subject terms: Gabor filters, texture segmentation, statistical image analysis, texture analysis, computer vision, image segmentation

## I. INTRODUCTION

Gabor filters have been used in many applications, such as texture segmentation [1]–[10], target detection [11], [12], fractal dimension measurement [13], document analysis [14], edge detection [15], retina identification [16], image coding [17], [18], and image representation [19]. Further, Gabor filters have been shown to possess optimal filter properties and to have similarities to biological vision systems [20]. Despite considerable research activity, the design of single or multiple Gabor filters to segment multiple textures remains an open issue. In the following, we present a method to address the single-filter multi-texture Gabor filter design problem. This development lays the groundwork for ongoing development of a multi-texture multi-filter design method [9]. A comprehensive general overview of Gabor filters is provided in the references [2], [5].

A basic *Gabor filter channel* typically uses a *Gabor prefilter* and a *Gaussian postfilter*, [21] as illustrated in Fig. 1 and discussed in Section 2. A fundamental issue confronted by the aforementioned efforts [1]–[8], [11]–[19], [22] is *how the Gabor prefilters and Gaussian postfilters are to be designed and selected*. Two main methods have been pro-

posed previously for selecting Gabor prefilters for texture segmentation: the *filter-bank* approach and the *filter-design* approach.

Many filter-bank approaches have been proposed. Daugman considered a filter-bank wavelet decomposition based on biological vision [17]. A subset of a similar filter bank was proposed by Jain and Farrokhnia [3]. Other filter banks were proposed by Turner [23], Randen and Husøy [24], Malik and Perona [25], Bigün and du Buf [6], [26], and Chang and Kuo [27]. One difficulty with this approach is that the filter parameters are preset *ad hoc* and are not necessarily optimal for a particular processing task. In addition, some segmentation tasks may not require a large bank of filters for effective performance or may not tolerate the large computational burden imposed by a large filter bank. A final difficulty is that a large bank of filters produces an output feature-vector with a large number of dimensions. While efforts have been made to reduce this dimensionality [3], [6], potential difficulties with a complicated classifier and the “curse of dimensionality” remain [28].

The filter-design approach focuses on designing one or a few filters for a particular application in an effort to reduce the difficulties of filter-bank approaches [1], [2], [5], [7], [8], [21]. Several filter-design approaches have been proposed previously. In the first approach, Bovik *et al.* presented a design approach that used one Gabor filter per texture [1], [2]. The center frequency of each prefilter was selected to correspond to a peak in the texture power spectrum, and prefilter bandwidths were determined by the center frequency. Tan proposed a similar filter-design scheme where a spectral peak determined the filter center frequency [10]. In another approach, Dunn *et al.* provided a detailed treatment of the optimal design of a single Gabor prefilter for segmenting two textures [5], [7]. The method involved an exhaustive search to find the prefilter center frequency, using measured output statistics and a Rician statistical model. Using measured Rician statistics, the image-segmentation error was estimated and the prefilter with the lowest error was selected. In the final approach, Weldon *et al.* developed a more computationally efficient filter-design technique based on the average energies of the prefiltered textures [8], [21].

Limitations remain, however, in the filter-design approaches above. First, the methods of Bovik *et al.* do not attempt to maximize the use of a single prefilter; i.e., these methods give a filter that discriminates a single texture rather than several textures [1], [2]. Second, prior methods of the present authors are limited to the design of a single

Department of Electrical Engineering, University of North Carolina at Charlotte, Charlotte, NC 28223, E-mail: tpweldon@uncc.edu

<sup>†</sup>Department of Electrical Engineering, The Pennsylvania State University, University Park, Pennsylvania 16802

<sup>††</sup>Department of Computer Science and Engineering, The Pennsylvania State University, University Park, Pennsylvania 16802 Copyright 1996 Society of Photo-Optical Instrumentation Engineers. This paper was published in Optical Engineering October 1996 and is made available as an electronic preprint with permission of SPIE. One print or electronic copy may be made for personal use only. Systematic or multiple reproduction, distribution to multiple locations via electronic or other means, duplication of any material in this paper for a fee or for commercial purposes, or modification of the content of the paper are prohibited.

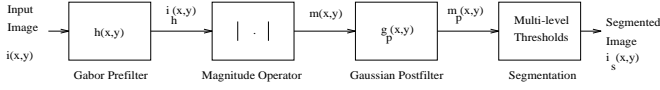


Fig. 1. Image processing diagram.

prefilter for segmenting a bipartite (two-texture) image [5], [7], [8]. Third, an explicit methodology has not been suggested for selecting an appropriate Gaussian postfilter in concert with an effective Gabor prefilter. Finally, the previous methods do not strictly provide a complete unified mathematical framework for estimating all necessary parameters.

We present a novel approach for designing a single Gabor filter to segment multiple textures ( $\geq 2$ ) in images. The approach results in a precise, unified, and computationally efficient method for determining Gabor prefilter and Gaussian postfilter parameters. Since the resulting Gabor prefilter can be used to segment more than two textures, we also propose a more general segmentation scheme. The overall result is a new mathematical framework that relates the texture power spectra, Gabor-prefilter parameters, nonlinear processing, Gaussian postfiltering, output statistics, and image-segmentation error. This framework provides an important bridge to the more general multi-filter, multi-texture segmentation problem, as discussed in related ongoing research [9], [29], [30].

The remainder of this paper proceeds as follows. Section 2 first reviews the image-processing scenario. In Section 3, we present the new Gabor-filter design technique. Section 4 presents results demonstrating the efficacy of the proposed methods.

## II. PROBLEM OVERVIEW

Before proceeding, we briefly outline the steps in processing an image. These processing steps are outlined in the diagram of Fig. 1. More detail can be found in the references [2], [21].

The input image  $i(x, y)$  is assumed to be composed of disjoint regions of  $\mathcal{N}$  different textures  $t_i(x, y), i = 1, \dots, \mathcal{N}$ . First, the input  $i(x, y)$  is filtered using a bandpass Gabor prefilter having an impulse response  $h(x, y)$ :

$$\begin{aligned} h(x, y) &= g(x, y) e^{-j2\pi(Ux+Vy)} \\ &= \frac{1}{2\pi\sigma_g^2} e^{-\frac{(x^2+y^2)}{2\sigma_g^2}} e^{-j2\pi(Ux+Vy)} \end{aligned} \quad (1)$$

with 2-D Fourier transform

$$\begin{aligned} H(u, v) &= G(u - U, v - V) \\ &= e^{-2\pi^2\sigma_g^2((u-U)^2+(v-V)^2)}, \end{aligned} \quad (2)$$

where  $G(u, v)$  is the Fourier transform of the Gaussian  $g(x, y)$ . In (1) and (2), parameters  $(U, V, \sigma_g)$  determine the *Gabor prefilter*. The parameters  $(U, V)$  are referred to as the prefilter *center frequency*, and parameter  $\sigma_g$  determines the prefilter bandwidth. For simplicity, the Gaussian envelope  $g(x, y)$  is taken to be a symmetric function [21].

Continuing with Fig. 1, the output of the prefilter  $i_h(x, y)$  is

$$i_h(x, y) = h(x, y) * i(x, y) \quad (3)$$

where  $*$  denotes convolution in two dimensions. The magnitude of the generally complex-valued first-stage output is computed in the second stage as

$$m(x, y) = |i_h(x, y)| = |h(x, y) * i(x, y)|, \quad (4)$$

where  $m(x, y)$  is shown in Section 3.1 to have approximately Rician statistics within the extent of each texture. A Gaussian *postfilter*  $g_p(x, y)$  is applied to smooth the prefilter output  $m(x, y)$  yielding the postfiltered image

$$\begin{aligned} m_p(x, y) &= m(x, y) * g_p(x, y) \\ &= m(x, y) * \frac{1}{2\pi\sigma_p^2} e^{-\frac{(x^2+y^2)}{2\sigma_p^2}}. \end{aligned} \quad (5)$$

The subscript  $p$  on  $\sigma_p$  denotes the postfilter parameter in (5), while the subscript  $g$  on  $\sigma_g$  was used previously to denote the Gabor prefilter parameter in (1).

We refer to  $i_h(x, y)$  as the *prefiltered image*,  $m(x, y)$  as the *prefilter output*, and  $m_p(x, y)$  as the *postfilter output*. The postfiltering in (5) has been used by previous investigators to smooth out variations in  $m(x, y)$  due to fluctuations in the underlying texture or noise in the image [1], [5], [7]. Thus,  $m_p(x, y)$  has a smaller variance than  $m(x, y)$ , and, therefore, results in better discrimination between different textures [8], [31].

As a final processing step, the segmented image  $i_s(x, y)$  is generated by applying several optimal thresholds to the postfiltered image  $m_p(x, y)$ . More elaborate methods can be used to generate the segmented image from the postfiltered image, but a simple threshold scheme more directly illustrates the effectiveness of the new methods.

Given the system of Fig. 1, the goal is to *design the Gabor prefilter  $h(x, y)$  and Gaussian postfilter  $g_p(x, y)$  such that the resulting total segmentation error for all texture classes in  $m_p(x, y)$  is minimized.*

## III. FILTER DESIGN METHOD

This section presents a filter-design method that addresses the general design goal stated above. Before proceeding, we present a statistical development that leads to the proposed method. To this end, we first discuss a model for a prefiltered texture and an associated local spectral model for an unfiltered input texture (Section 3.1). Using these models and two different Gabor-filter envelope scales, we derive a relationship between the texture power spectrum and the parameters that characterize the Rician pdf of the prefilter output (Section 3.2). The predicted Rician statistics of the prefilter output are then used to predict the Gaussian postfilter output statistics (Section 3.3). Finally, optimal segmentation thresholds and the associated segmentation error are calculated for the postfiltered output (Section 3.4). The filter design is then established by selecting the filter associated with the minimum predicted error, as described in Section 3.5. Section 3.6 discusses computational issues.

### A. The Rician Model

In this section, the statistical models of the Gabor prefiltered textures are developed. The following development tends to focus on a single constituent texture  $t_i$  but generally applies to all  $\mathcal{N}$  constituent textures in the image.

We first extend recent results by Dunn and Higgins that have shown the prefilter output to be characterized well by a Rician distribution [7]. We retain the 1-dimensional notation of Dunn and Higgins for simplicity, and represent the Gabor prefiltered output  $i_h(x, y)$  as  $i_h(x)$ . The 1-dimensional results are then generalized to the 2-dimensional case. A Gabor prefiltered texture with random perturbations is modeled by [7], [8], [32]

$$i_h(x) = [(A_0 \cos(\theta) + X(x)) + j(A_0 \sin(\theta) + Y(x))] e^{j2\pi(Ux)}, \quad (6)$$

where the sinusoidal component of the Gabor prefiltered image has magnitude  $A_0$  and frequency  $U$ . This sinusoidal component is due to the unperturbed texture. The independent, zero-mean, Gaussian lowpass random processes  $X(x)$  and  $Y(x)$  are due to the perturbations in the texture. Eq. (6) can also be written as

$$i_h(x) = A_0 e^{j2\pi Ux + \theta} + (X(x) + jY(x)) e^{j2\pi(Ux)}. \quad (7)$$

In two dimensions, the model for the Gabor prefiltered image becomes

$$\begin{aligned} i_{h_i}(x, y) &\approx s_i(x, y) + n_i(x, y) \\ &= A_i e^{j2\pi(u_i x + v_i y)} + n_i(x, y) \end{aligned} \quad (8)$$

where  $i_{h_i}(x, y)$  represents the image prefiltered by  $h(x, y)$  for input texture  $t_i(x, y)$ , and  $(u_i, v_i)$  is the frequency of the sinusoidal component of the prefiltered image. From (8), the Gabor prefiltered image is then comprised of a complex exponential  $s_i(x, y) = A_i e^{j2\pi(u_i x + v_i y)}$ , and bandpass noise  $n_i(x, y)$ . The phase term  $\theta$  is dropped in (8) since the locations of different textures in the input image are usually unknown, and our methods do not use phase information. Finally, Eq. (8) applies to each texture  $t_i$ , so there are  $\mathcal{N}$  prefiltered textures  $i_{h_i}(x, y)$  corresponding to the responses of a single filter  $h(x, y)$  to each of the  $\mathcal{N}$  textures.

The magnitude of the complex signal  $i_{h_i}(x, y)$  was shown to have a Rician distribution  $p_i(m)$  when  $n_i(x, y)$  is Gaussian bandlimited noise; i.e.,

$$p_i(m) = \frac{2m}{N_i} e^{-\left(\frac{m^2 + A_i^2}{N_i}\right)} I_0\left(\frac{2mA_i}{N_i}\right) \quad (9)$$

where  $A_i$  is the amplitude of the complex exponential in (8),  $N_i$  is the total noise power,  $m \in m_i(x, y)$ , and  $I_0(\cdot)$  is the modified Bessel function of the first kind with zero order [7], [33]–[35]. The Rician distribution is completely determined by the values of  $A_i$  and  $N_i$ . For  $A_i^2 \ll N_i$ , the Rician model in (9) also accommodates situations in which the output statistics follow a Rayleigh distribution. The ability to accommodate a Rayleigh distribution is important, since the filtered textures, in practice, commonly have a Rayleigh distribution. One likely reason for this is

that it is unlikely that all textures will have a dominant sinusoid, or equivalently large  $A_i$ , at the center frequency of a single filter.

Given the filtered-texture model in (8), we next consider the *local* frequency spectrum at the *input* of the Gabor prefilter. The bandpass Gabor prefilter  $h(x, y)$  passes spatial frequencies localized around the center frequency  $(U, V)$  and rejects energy at other frequencies. Thus, a *locally* equivalent spatial-frequency model at the *input* of the prefilter is a complex exponential plus white noise, with power spectral density  $S_i(u, v)$ :

$$S_i(u, v) \approx A_i^2 \delta(u - u_i, v - v_i) + \frac{\eta_i}{4} \quad (10)$$

where  $(u_i, v_i)$  and  $A_i$  are the frequency and amplitude of the dominant sinusoid within the passband of the Gabor prefilter with parameters  $(U, V, \sigma_g)$ . The impulse  $\delta(\cdot)$  in the power spectrum models the dominant sinusoid within the filter passband, and the remaining power in the passband is allocated to  $\eta_i/4$ . In essence, we consider  $i_{h_i}(x, y)$  from (8) to be the prefiltered version of the power spectrum of a correlation-ergodic process in (10) [36]. The model (10), is only valid within the approximate passband of the prefilter; i.e., it is a *local* spatial-frequency model for an input texture  $t_i(x, y)$ . We emphasize that (10) represents the *input* to the filter, and thus the noise term  $\frac{\eta_i}{4}$  is bandlimited at the *output* of the filter.

### B. Estimation of Rician Parameters

We proceed to develop an estimate of the Rician parameters  $A_i$  and  $N_i$  in (9) for texture  $t_i$  as a function of the Gabor prefilter parameters  $(U, V, \sigma_g)$  and the texture power spectrum  $S_i(u, v)$ . We begin by observing that  $A_i^2 + N_i$  equals the total power at the output of the Gabor prefilter. Hence, we consider a measure of the Gabor-prefilter output power for determining  $A_i$  and  $N_i$ . We then need to solve for two Rician parameters,  $A_i$  and  $N_i$ . So, we use the Gabor prefilter output power at two envelope scales to solve for  $A_i$  and  $N_i$ . Finally, we use an FFT to efficiently generate estimates of these parameters at all discrete FFT frequencies.

When texture  $t_i(x, y)$  is filtered by a Gabor prefilter  $h(x, y)$  with fixed parameters  $(U, V, \sigma_g)$ , the prefilter output power  $P_i(U, V, \sigma_g)$ , using (2), is

$$P_i(U, V, \sigma_g) = \int_{-\infty}^{\infty} \int_{-\infty}^{\infty} S_i(u, v) |G(u - U, v - V)|^2 dudv. \quad (11)$$

As shown in the Appendix,  $P_i(U, V, \sigma_g)$  can be calculated efficiently for all Gabor prefilter center frequencies  $(U, V)$  simultaneously using the form

$$\begin{aligned} P_i(u, v, \sigma_g) &= \mathcal{F} \{ g(x, y) * g(x, y) R_i(x, y) \} \\ &= |G(u, v)|^2 * S_i(u, v) \end{aligned} \quad (12)$$

where  $\mathcal{F}\{\cdot\}$  denotes the Fourier transform. A fast Fourier transform (FFT) is used to implement the convolution. The FFT implementation then gives  $P_i(u, v, \sigma_g)$  at a discrete set of center frequencies  $(u, v)$  for a particular  $\sigma_g$ .

Given (10) and (12), the Rician parameters  $A_i$  and  $N_i$  may be estimated from  $P_i(u, v, \sigma_g)$ . When the input spectral model (10) is substituted into (12), we obtain the following measure of prefilter output power as a function of prefilter center frequency:

$$P_i(u, v, \sigma_g) \approx |G(u, v)|^2 * S_i(u, v) \approx A_i^2 e^{-4\pi^2 \sigma_g^2 [(u-u_i)^2 + (v-v_i)^2]} + \frac{\eta_i}{16\pi\sigma_g^2}. \quad (13)$$

The first term above arises from the dominant sinusoid in the passband represented by the impulse in (10). The second term represents the remaining power in the prefiltered image  $i_{hi}(x, y)$  and gives the parameter  $N_i = \eta_i/(16\pi\sigma_g^2)$  in the Rician pdf  $p_i(m)$  in (9) [8], [31].

If we next consider  $P_i(u, v, \sigma_g)$  at two prefilter envelope scales set by  $\sigma_{g\alpha}$  and  $\sigma_{g\beta}$ , we may solve for  $A_i$  and  $N_i$  at the frequency  $(u_i, v_i)$  of the dominant sinusoid:

$$\begin{aligned} P_i(u_i, v_i, \sigma_{g\alpha}) &\approx A_i^2 + \frac{\eta_i}{16\pi\sigma_{g\alpha}^2} \\ &= A_i^2(u_i, v_i, \sigma_{g\alpha}) + N_i(u_i, v_i, \sigma_{g\alpha}) \\ P_i(u_i, v_i, \sigma_{g\beta}) &\approx A_i^2 + \frac{\eta_i}{16\pi\sigma_{g\beta}^2} \\ &= A_i^2(u_i, v_i, \sigma_{g\alpha}) + N_i(u_i, v_i, \sigma_{g\alpha}) \left(\frac{\sigma_{g\alpha}}{\sigma_{g\beta}}\right)^2. \end{aligned} \quad (14)$$

Rearranging (14) gives

$$A_i^2(u_i, v_i, \sigma_{g\alpha}) \approx P_i(u_i, v_i, \sigma_{g\alpha}) - N_i(u_i, v_i, \sigma_{g\alpha}). \quad (15)$$

and

$$N_i(u_i, v_i, \sigma_{g\alpha}) \approx \frac{P_i(u_i, v_i, \sigma_{g\alpha}) - P_i(u_i, v_i, \sigma_{g\beta})}{[1 - (\frac{\sigma_{g\alpha}}{\sigma_{g\beta}})^2]}. \quad (16)$$

As the prefilter center frequency diverges from  $(u_i, v_i)$ , the exponential term in (13) becomes less than 1, and an error term is introduced in (14-15), particularly for  $\eta_i = 0$ . (Note that for  $A_i = 0$ , this error does not arise.) Examination of (13), (15), and (16) for  $\eta_i = 0$  shows that as the exponential term in (13) becomes less than 1, power is increasingly attributed to  $N_i$ , when in fact  $N_i$  should equal 0. The net effect of this error, fortunately, is not detrimental in the overall algorithm. The error induces a preference for the frequency  $(u_i, v_i)$  of the local dominant sinusoid, since lower  $N_i$  implies lower variance in  $m_p(x, y)$ . Also, the error is bounded by the following constraint that relates the prefiltered image power and the Rician parameters:

$$P_i(u, v, \sigma_{g\alpha}) = A_i^2(u, v, \sigma_{g\alpha}) + N_i(u, v, \sigma_{g\alpha}). \quad (17)$$

Hence, the following equations are used to estimate  $A_i$  and  $N_i$  for all candidate Gabor prefilter center frequencies  $(u, v)$ :

$$A_i^2(u, v, \sigma_{g\alpha}) \approx P_i(u, v, \sigma_{g\alpha}) - N_i(u, v, \sigma_{g\alpha}), \quad (18)$$

and

$$N_i(u, v, \sigma_{g\alpha}) \approx \frac{P_i(u, v, \sigma_{g\alpha}) - P_i(u, v, \sigma_{g\beta})}{[1 - (\frac{\sigma_{g\alpha}}{\sigma_{g\beta}})^2]} \quad (19)$$

where we reserve the upper case  $(U, V)$  for the constant parameters of the final designed filter and use lower case  $(u, v)$  to indicate function variables in (18) and (19).

### C. Postfiltering

The two preceding subsections established for each texture  $t_i$  the relationship between the Gabor prefilter parameters  $(u, v, \sigma_g)$ , the texture power spectra  $S_i(u, v)$ , and the pdf of the prefilter output  $m_i(x, y)$ . The next two subsections consider postfiltering, thresholding, and segmentation error. We first use the prefilter output statistics to estimate the postfilter output statistics. Then, we compute optimal thresholds and the associated segmentation error, using the predicted postfilter output statistics. Finally, the prefilter and postfilter parameters associated with the minimum error are selected.

First, the postfilter output statistics are established. Since  $A_i$  and  $N_i$  determine the Rician pdf, the means  $\mu_{g_i}(\cdot)$  and variances  $s_{g_i}^2(\cdot)$  of the prefilter output  $m_i(x, y)$  may be calculated directly for each sample texture  $t_i(x, y)$ . This is done for each of the  $\mathcal{N}$  sample textures as a function of  $(u, v, \sigma_{g\alpha})$  using  $A_i^2(u, v, \sigma_{g\alpha})$  from (18) and  $N_i(u, v, \sigma_{g\alpha})$  from (19):

$$\begin{aligned} \mu_{g_i}(u, v, \sigma_{g\alpha}) &= \int_0^\infty m \frac{2m}{N_i(u, v, \sigma_{g\alpha})} e^{-\left(\frac{m^2 + A_i^2(u, v, \sigma_{g\alpha})}{N_i(u, v, \sigma_{g\alpha})}\right)} I_0\left(\frac{2mA_i(u, v, \sigma_{g\alpha})}{N_i(u, v, \sigma_{g\alpha})}\right) dm \\ s_{g_i}^2(u, v, \sigma_{g\alpha}) &= \int_0^\infty \frac{(m - \mu_{g_i}(u, v, \sigma_{g\alpha}))^2 2m}{N_i(u, v, \sigma_{g\alpha})} e^{-\left(\frac{m^2 + A_i^2(u, v, \sigma_{g\alpha})}{N_i(u, v, \sigma_{g\alpha})}\right)} I_0\left(\frac{2mA_i(u, v, \sigma_{g\alpha})}{N_i(u, v, \sigma_{g\alpha})}\right) dm. \end{aligned} \quad (20)$$

The means  $\mu_{p_i}(\cdot)$  and variances  $s_{p_i}^2(\cdot)$  of the postfilter output  $m_{p_i}(x, y)$  are derived from the prefilter means and variances using the parameters  $\sigma_g$  and  $\sigma_p$ . From (5), the postfiltering produces a spatial averaging of  $m_i(x, y)$ . The means  $\mu_{p_i}(\cdot)$  and variances  $s_{p_i}^2(\cdot)$  of the postfiltered outputs are then approximated as:

$$\begin{aligned} \mu_{p_i}(u, v, \sigma_{g\alpha}) &\approx \mu_{g_i}(u, v, \sigma_{g\alpha}) \\ s_{p_i}^2(u, v, \sigma_{g\alpha}, \sigma_p) &\approx \frac{s_{g_i}^2(u, v, \sigma_{g\alpha}) \sigma_{g\alpha}^2}{\sigma_p^2}; \quad \sigma_{g\alpha}^2 < \sigma_p^2 \end{aligned} \quad (21)$$

For small ratios of  $\sigma_{g\alpha}^2/\sigma_p^2$ , the postfiltered output pdf will become approximately Gaussian, per the central limit theorem. In addition, the Rician distribution itself approaches a Gaussian distribution for  $A_i^2 \gg N_i$ . Therefore, the pdf  $p_i(\cdot, m_p)$  of the postfilter output  $m_{p_i}(x, y)$  is approximated for texture  $t_i$  as

$$p_i(u, v, \sigma_{g\alpha}, \sigma_p, m_p) \approx \frac{1}{\sqrt{2\pi s_{p_i}^2(u, v, \sigma_{g\alpha}, \sigma_p)}} e^{-\frac{(m_p - \mu_{p_i}(u, v, \sigma_{g\alpha}, \sigma_p))^2}{2s_{p_i}^2(u, v, \sigma_{g\alpha}, \sigma_p)}} \quad (22)$$

where  $m_p \in m_{p_i}(x, y)$ .

The effect of postfiltering is particularly pronounced when the prefilter output is Rayleigh distributed; i.e., the Rician distribution approaches a Rayleigh distribution for  $A_i^2 \ll N_i$ . In our experience, the Rayleigh case is common in filtered textures. The longer tails on the Rayleigh distribution, relative to a Rician, lead to larger image-segmentation errors when postfiltering is not employed.

The inclusion of postfiltering in the proposed method enables a balanced treatment of Rician and Rayleigh distributed prefilter outputs. It also offers a new perspective on the need for postfiltering.

#### D. Segmentation

Having established the postfilter output pdf's, a series of optimal segmentation thresholds are calculated based on equal *a priori* probabilities for the textures and the resulting Gaussian pdf's at the postfilter output. Bayesian thresholds are selected that minimize the total segmentation error. These thresholds are set so that  $m_p(x, y)$  is assigned to the texture whose probability density is largest for a given output level. This approach to texture segmentation can be viewed as a local classifier [32]. With equal *a priori* probabilities for the  $\mathcal{N}$  textures, the minimum segmentation error rate is achieved by deciding texture  $t_i$  when [28]:

$$p_i(u, v, \sigma_{g\alpha}, \sigma_p, m_p) > p_j(u, v, \sigma_{g\alpha}, \sigma_p, m_p); \quad j \neq i, 1 \leq i, j \leq \mathcal{N} \quad (23)$$

where the estimated Gaussian pdf  $p_i(\cdot, m_p)$  of the postfiltered output  $m_{p_i}(x, y)$  for texture  $t_i(x, y)$  is:

$$p_i(u, v, \sigma_{g\alpha}, \sigma_p, m_p) = \frac{1}{\sqrt{2\pi s_{p_i}^2(u, v, \sigma_{g\alpha}, \sigma_p)}} e^{-\frac{(m_p - \mu_{p_i}(u, v, \sigma_{g\alpha}, \sigma_p))^2}{2s_{p_i}^2(u, v, \sigma_{g\alpha}, \sigma_p)}} \quad (24)$$

Equation (24) is implemented by first solving for the points at which  $p_i(\cdot, m_p) = p_j(\cdot, m_p)$  for  $j \neq i$ . Since the postfiltered outputs are assumed to have Gaussian pdf's, the two roots are found by solving a simple quadratic equation. The thresholds occur at the points at which the pdf's are equal:

$$\frac{1}{\sqrt{2\pi s_{p_i}^2(\cdot)}} e^{-\frac{(m_p - \mu_{p_i}(\cdot))^2}{2s_{p_i}^2(\cdot)}} = \frac{1}{\sqrt{2\pi s_{p_j}^2(\cdot)}} e^{-\frac{(m_p - \mu_{p_j}(\cdot))^2}{2s_{p_j}^2(\cdot)}} \quad (25)$$

taking the logarithm of both sides and rearranging:

$$\frac{(m_p - \mu_{p_j}(\cdot))^2}{2s_{p_j}^2(\cdot)} - \frac{(m_p - \mu_{p_i}(\cdot))^2}{2s_{p_i}^2(\cdot)} = \ln \left( \frac{s_{p_i}(\cdot)}{s_{p_j}(\cdot)} \right) \quad (26)$$

This quadratic in  $m_p$  is solved for the two thresholds [37]. Each pair of pdf's, corresponding to a pair of textures, results in two roots. The  $\mathcal{N}^2 - \mathcal{N}$  thresholds  $\tau_q, q = 1, \dots, \mathcal{N}^2 - \mathcal{N}$  associated with (26) are then re-ordered such that  $\tau_1 < \tau_2 < \dots < \tau_{\mathcal{N}^2 - \mathcal{N}}$ . Fig. 2 illustrates the case of six thresholds associated with three Gaussian pdf's (i.e., three input textures). Values of  $m_p(x, y)$  in the interval  $[\tau_r, \tau_{r+1})$  are assigned to texture  $t_\varepsilon$  if:

$$p_\varepsilon(u, v, \sigma_{g\alpha}, \sigma_p, m_p(x, y)) > p_\zeta(u, v, \sigma_{g\alpha}, \sigma_p, m_p(x, y)) \quad \text{for all } \zeta \neq \varepsilon \quad (27)$$

for any fixed combination of  $(u, v, \sigma_{g\alpha}, \sigma_p)$ .

Note that  $m_p > 0$  and we may further restrict the thresholds to include only  $\tau > 0$ , thus eliminating negative thresholds which may be induced by negative values

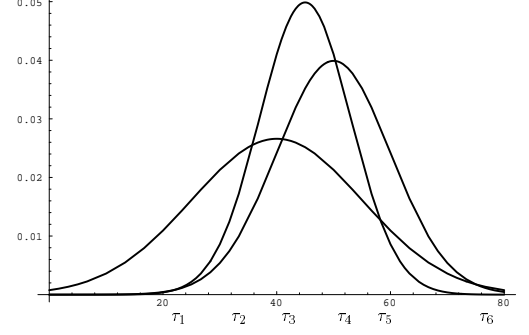


Fig. 2. Three Gaussian pdf's with 6 associated thresholds. Each pdf represents the postfiltered output statistics for a different texture.

of the Gaussian pdf. The set of thresholds is also extended as required to include the intervals  $[0, \tau_1)$  and  $[\tau_{\mathcal{N}^2 - \mathcal{N}}, \infty)$ . Using these thresholds, the segmentation error  $e_s(\cdot)$  is given as:

$$e_s(u, v, \sigma_{g\alpha}, \sigma_p) \approx 1 - \frac{1}{\mathcal{N}} \sum_r \int_{\tau_r}^{\tau_{r+1}} p_\varepsilon(u, v, \sigma_{g\alpha}, \sigma_p, m_p) dm_p \quad (28)$$

for any fixed combination of  $(u, v, \sigma_{g\alpha}, \sigma_p)$  and where  $p_\varepsilon(\cdot)$  is the pdf associated with texture  $t_\varepsilon$  assigned to the interval  $[\tau_r, \tau_{r+1})$ .

#### E. Filter Design

The resulting estimate of segmentation error in (28) is used as the basis for the design of the system in Fig. 1. The best filter design for any fixed  $(\sigma_{g\alpha}, \sigma_p)$  minimizes the predicted error in (28) as a function of Gabor-filter center frequency  $(u, v)$ :

$$(U, V) = \arg \left\{ \min_{(u, v)} [e_s(u, v, \sigma_{g\alpha}, \sigma_p)] \right\}, \quad \text{for any } (\sigma_{g\alpha}, \sigma_p). \quad (29)$$

For guidelines on selecting values for  $\sigma_{g\alpha}$ , see Dunn *et al.* [5]. The value of  $\sigma_p$  is in most cases larger than  $\sigma_{g\alpha}$ , but not so large that the desired resolution of the segmentation becomes unacceptable. A range of parameter values are used later in the experimental results to illustrate the performance of the algorithm and to suggest appropriate parameter ranges. Our results show that we produce effective estimates of the output pdf's for each texture, thus providing effective statistical estimates for texture classification within any given textured region.

##### E.1 Filter Design Algorithm

Our *complete filter-design approach* can now be summarized.

1. Given samples of the textures of interest  $t_i(x, y)$ ,  $i = 1, \dots, N$ , estimate the associated Rician statistics of  $m_i(x, y)$  for each texture using (18) and (19), over a range of Gabor filter center frequencies  $(u, v)$  at an appropriately selected scale  $\sigma_g$ .
2. Estimate the statistics of the postfilter output  $m_{p_i}(x, y)$  using the results generated in step 1 and (21). This gives a Gaussian distributed  $m_{p_i}(x, y)$  for each  $t_i$  per (22).
3. Compute a series of optimal thresholds using (26) that can be applied to  $m_p(x, y)$  and compute the associated segmentation error assuming equal *a priori* probabilities for each texture per (28).
4. Select the Gabor prefilter, determined by  $(U, V, \sigma_g)$ , and Gaussian postfilter, determined by  $\sigma_p$ , that provide lowest image-segmentation error.

The overall spatial resolution of the system of Fig. 1 is set by the combination of  $\sigma_{g\alpha}$  and  $\sigma_p$ . Direct minimization of (29) for all four parameters leads to unsatisfactory spatial resolution because the error  $e_s(\cdot)$  tends to decrease as  $\sigma_{g\alpha}$  and  $\sigma_p$  increase. One possible modification is to add some measure of expected segmentation error due to loss of spatial resolution. This modification is beyond the scope of the present work and the topic of related research [9].

#### F. Computational Efficiency

A significant advantage of the proposed filter-design algorithm is that it is computationally more efficient than a similar approach by Dunn and Higgins [7]. Admittedly, this computational efficiency may not be critical in the design of a single filter, but it does become a critical issue when the number of possibilities undergoes a combinatorial increase for the design of multiple filters [9], [29]. Thus, the efficiencies gained in the present single-filter design procedure will become increasingly important in the development of multi-filter design methods [9], [29]. These improvements in computational efficiency also are important in interactive filter-design applications where slow algorithms and lengthy computation times may be unacceptable.

The computational complexity of the new method is in large part driven by the computation of  $P(u, v)$  in (12) for each of the  $N$  sample textures. First,  $R_i(x, y)$  is computed as a size  $N \times N$  cyclic autocorrelation using the operation  $\mathcal{F}^{-1}\{|\mathcal{F}\{t_i\}|^2\}$  where  $t_i$  is the size  $N \times N$  sample texture. Second,  $P(u, v)$  is calculated as  $\mathcal{F}\{w(x, y)R_i(x, y)\}$  using an  $N \times N$  window for  $w(x, y)$ . These two steps are implemented as three  $N \times N$  FFT's with a computational complexity of  $\approx 3N^2 \log_2 N$ .

The most direct comparison in computational complexity is with the work of Dunn and Higgins, since this is the only other approach that considers the design of a single filter and uses segmentation-error criteria for designing the filter [7]. The computational complexity of this approach is primarily driven by the need to per-

form  $\approx 200$  2-dimensional Gaussian-windowed FFT's (Fast Fourier Transforms) on each sample texture  $t_i$ . This results in a computational complexity of  $\approx 200N^2 \log_2 N$  for size  $N \times N$  sample texture images. Thus, the new method is approximately 60 times more efficient than the method of Dunn and Higgins. This may be somewhat overstated since the extremely low computational expense related to FFT's in the new method makes the computational expense of other tasks more significant. Nevertheless, there is a significant reduction in computation.

#### IV. RESULTS

The proposed algorithms were tested on a range of Brodatz and synthetic texture images [38]. All images used were  $256 \times 256$  pixel 8-bit gray-scale images. The mean values of all textures were equalized so that segmentation based on average gray scale was not possible. In each example a single value of  $\sigma_g$  and  $\sigma_p$  are used to illustrate the effectiveness of the selected prefilter center-frequency and the accuracy of output statistical estimates. For guidelines on selecting values for  $\sigma_g$ , see Dunn *et al.* [5]. In the following examples, several values for  $\sigma_g$  and  $\sigma_p$  are used to demonstrate performance of the method for variation in these two parameters.

We first start with a two-texture example that is later compared to the two-texture Gabor-filter design method of Dunn and Higgins [7]. Fig. 3 presents results for a pair of Brodatz textures using the Gabor prefilter designed with the new algorithm. The  $256 \times 256$  input image  $i(x, y)$  in Fig. 3(a) consists of a central d77 "cotton canvas" texture region superimposed on a background of the d16 "herringbone weave" texture. The prefilter output  $m(x, y)$  is shown in Fig. 3(b) for  $\sigma_g = 5$ . The postfilter output  $m_p$  is shown in Fig. 3(c) with  $\sigma_p = 10$ .

Fig. 3(d) is a plot of the predicted segmentation error as a function of Gabor prefilter center frequency  $(u, v)$ . The intensity is linearly proportional to the segmentation error, with a white intensity indicating a segmentation error of 100% and black 0%. The circular appearance of Fig. 3(d) is due to a lowpass filter operation on each of the original Brodatz images to eliminate high frequency artifacts [39]. The darkest point in the image, enclosed in the white box at  $(U, V) = (.004, -.176)$  cycles per pixel, corresponds to the center frequency of the designed Gabor prefilter. The particular frequency half-plane selected is a function of numerical precision; it is apparent from the conjugate symmetry of the Fourier transform and from the plot of segmentation error as a function of center frequency that the error at a center frequency  $(u, v)$  is equal to the error at  $(-u, -v)$ .

To illustrate the effect of postfiltering on the overall segmentation, the prefilter output in Fig. 3(b) is shown segmented in Fig. 3(e). The segmentation thresholds for the prefilter output are selected in a manner similar to that outlined in (23) for the postfiltered image, except that the predicted Rician pdf's of the prefilter output are used in place of the predicted Gaussian pdf's of the postfilter output. The segmented postfilter output is shown in Fig. 3(f)

using the optimal thresholds from (23). The postfiltering is seen to reduce the sporadic misclassifications seen within the two textured regions in (e).

The measured histograms of the prefilter output  $m(x, y)$  are shown in Fig. 4(a) as solid lines, and the predicted Rician pdf's using (9) are shown as dashed lines. The curves that peak at lower output amplitude correspond to the dark inner region of Fig. 3(b), and the curves that peak at the larger amplitude correspond to the bright outer border of Fig. 3(b). The lower amplitude histogram has a Rayleigh appearance, while the upper distribution has a more Gaussian appearance characteristic of large  $A^2$  relative to  $N$  in (9). The differences in the appearance of the two pdf's is confirmed by the predicted values of  $A^2/N = 0.4$  and  $A^2/N = 3.57$  for the leftmost and rightmost histograms respectively.

The predicted Gaussian pdf (dashed lines) and measured output histograms (solid lines) are presented in Fig. 4(b) for the postfilter output  $m_p(x, y)$ . The postfiltering reduces the tails of the measured histograms, as is evident in comparing Fig. 4(a) to (b). A large amount of overlap is seen in the prefilter histograms of Fig. 4(a) and suggests the misclassifications evident in Fig. 3(e). The reduced histogram overlap after postfiltering suggests the reduction of sporadic misclassifications seen in Fig. 3(f).

Fig. 5 provides a comparison between the proposed method and that of Dunn and Higgins. In this figure, the predicted segmentation error is shown for the “d16-d77” example of Fig. 3, with intensity logarithmically proportional to error. The positive  $u$  and  $v$  axes are labeled, with  $(u, v) = (0, 0)$  at the center of the image. The white box surrounds the point at which the predicted segmentation error is minimized, and is the selected Gabor-filter center frequency. The “+” symbols overlaid on the plot are the most highly rated frequencies selected by the method of Dunn and Higgins. [7] In Fig. 5, the center frequencies selected by the Dunn and Higgins method occur near local minima in the error predicted by the present algorithm. Further, the center frequencies selected by the two design methods,  $(U, V) = (0, .195)$  and  $(U, V) = (.004, -.176)$ , do not differ greatly (ignoring the particular frequency half-plane selected).

The new method selects the Gabor prefilter center frequency with consideration of postfiltering effects, whereas Dunn and Higgins method does not include postfiltering effects [7]. Thus, the two algorithms do not necessarily select the same center frequencies. Both algorithms generate effective filters, and, as shown in Fig. 5, there is good agreement between predicted low error in the current method and the most highly ranked designs in Dunn and Higgins method. However, the present method offers significant computational advantages, includes postfiltering effects, is not restricted to pairs of textures, and directly leads to ongoing research on the design of multiple Gabor filters to segment multiple textures [9], [29].

A major advance of our method is that one filter can accommodate more than two textures. A three-texture

example is given in Fig. 6. The  $256 \times 256$  image in Fig. 6(a) is composed of two Brodatz textures and a bandlimited random texture. The image consists of a central region of texture d15 “straw” embedded in a larger region composed of d77 “cotton canvas” imposed on a background of lowpass-filtered uniformly-distributed random noise. Three  $256 \times 256$  samples of the textures were used to design the Gabor prefilter. The prefilter output  $m(x, y)$  is shown in Fig. 6(b) for the optimal Gabor filter with  $\sigma_g = 9$ . The mottled appearance of the bright outer border of Fig. 6(b) is characteristic of a Rayleigh distribution. A Rayleigh distribution is expected since the outer border corresponds to a bandpass version of the noise texture. The postfiltered image is provided in Fig. 6(c) with  $\sigma_p = 18$ . The spatial effect of postfiltering is most evident in the removal of the narrow black regions in the Rayleigh distributed outer border of Fig. 6(b).

The predicted error as a function of Gabor-prefilter center frequency  $(u, v)$  is shown in Fig. 6(d). The optimal center frequency is enclosed by the white box at  $(U, V) = (-.219, -.184)$  cycles per pixel. The plots of segmentation error suggest other good candidate Gabor-prefilter center frequencies may be located in other “dark basins” in Fig. 6(d) that have low segmentation error. The shape of the basins suggest filter orientations for asymmetric filters. Another interesting feature in the images is the “white ridges” separating the darker basins in error plots such as Fig. 6(d). These appear to correspond to “crossover frequencies” where the pdf for one texture is passing through the pdf of another texture, as the original lower-amplitude pdf becomes the larger amplitude pdf.

Fig. 6(e) is the segmented version of the prefilter output  $m_p(x, y)$ . The predicted (dashed lines) and actual (solid lines) histograms for  $m(x, y)$  are in Fig. 7(a) for each of the three constituent textures. Logarithmic coordinates are used because of the large dynamic range spanned by the three histograms on both axes. The large overlap in the three histograms suggests the misclassifications seen in Fig. 6(e). After postfiltering, the variance for each texture is reduced. The resulting reduction in the overlap of the three texture output distributions is seen in the postfilter output statistics of Fig. 7(b). The segmentation thresholds are set at the points at which the dashed lines of the three predicted pdf's intersect in Figs. 7 (b). The final segmentation is in Fig. 6(f).

Fig. 8 contains results for an image comprised of two synthetic textures plus one natural texture. The two synthetic textures are comprised of arrays of “+’s” and “L’s” and the natural texture is “cotton canvas.” As before, the prefilter output and postfilter output are in Figs. 8(b) and (c). The predicted error in Fig. 8(d) extends throughout the frequency plane since the synthetic textures do not require removal of undesired artifacts [39]. For this example, the only misclassifications in the prefilter-output segmentation occur at boundary discontinuities in Fig. 8(e). The reduction of within-region misclassifications is confirmed by the separation of the output distributions in Fig. 9(a)

and (b). The two larger amplitude distributions in these figures correspond to the two synthetic textures, while the lower distribution is for “cotton canvas.”

The extremely narrow measured distributions for the synthetic textures are due to the coherence and lack of randomness in these two textures. Although the predicted distributions for the two synthetic textures are wider than the measured distributions, the predicted means are representative of the estimated means and the distributions yield effective segmentation thresholds at the intersections of the pdf plots. While the overstatement of the variance in the predicted pdf's of synthetic textures may seem undesirable, the generation of extremely narrow predicted pdf's could be considered even more undesirable, since small variations in the mean value of the texture could displace the measured distribution significantly outside the predicted distribution. The narrowness of the measured synthetic texture pdf's also indicates that the prefiltered texture is a single sinusoid with little noise. The mechanisms causing over-estimation of variance for sinusoids are discussed elsewhere [9], but, as seen in Fig. 8 and Fig. 9, the predicted statistics remain useful for segmentation. In Fig. 8(f), the innermost region is apparently smaller than the corresponding textured region in (a). The displacement in the region boundary is due to conflicting requirements between the threshold required for optimum within-region classification and the threshold that minimizes boundary-localization error. The conflicting requirements are the topic of ongoing research [9], [29].

Finally, the results presented in this paper are for a single Gabor prefilter with a single Gaussian postfilter. Improved segmentation results are expected with multiple filters, and the present methods lead toward the implementation of a multi-filter multi-texture design procedure. The treatment of the single-filter multi-texture case, however, establishes much of the groundwork for a multi-filter multi-texture design method [9], [29].

## V. DISCUSSION

The proposed filter-design method constitutes a comprehensive treatment of the design of a single Gabor filter to segment multiple textures. The resulting Gabor prefilter design was shown to produce effective segmentations using a classifier based entirely on predicted output statistics. Further, the predicted output statistics were based on the frequency spectra of the sample textures (rather than samples of filtered textures) and included the effect of Gaussian postfiltering. The overall development and supporting results for the single-filter design provide important steps toward the development of a multi-filter design procedure in ongoing research [9], [29].

Finally, the previous discussion has focused on the design of Gabor filters. The methods, however, are applicable to other types of filters. This may be accomplished by replacing the kernel  $G(u, v)$  in (12) by a different kernel  $K(u, v)$  corresponding to the new filter type. The only caveat is that necessary properties of  $G(u, v)$  discussed in

the foregoing derivations set restrictions on  $K(u, v)$ .

## VI. APPENDIX: CALCULATION OF $P(u, v, \sigma_g)$

Below, we outline the steps leading to (12). This development is included for completeness and summarizes earlier results [8]. First, we let the input image  $i(x, y)$  be composed of disjoint regions of  $\mathcal{N}$  different textures,  $t_i(x, y)$ ,  $i = 1, \dots, \mathcal{N}$ . Further, we assume that we are given representative samples of the  $\mathcal{N}$  textures.

Denote the power spectral density of  $t_i(x, y)$  by  $S_i(u, v)$ . When texture  $t_i(x, y)$  is filtered by a Gabor prefilter  $h(x, y)$  with fixed parameters  $(U, V, \sigma_g)$ , the total output power of the prefiltered image  $i_h(x, y)$  is

$$P_i(U, V) = \int_{-\infty}^{\infty} \int_{-\infty}^{\infty} S_i(u, v) |H(u, v)|^2 du dv, \quad (30)$$

or

$$P_i(U, V) = \int_{-\infty}^{\infty} \int_{-\infty}^{\infty} S_i(u, v) |G(u - U, v - V)|^2 du dv.$$

Equation (30) provides the total output power of the Gabor prefiltered image  $i_h(x, y)$  for a particular Gabor prefilter and texture. The result in (30) leads to a more useful form where  $P_i(u, v)$  can be efficiently calculated for all Gabor prefilter center frequencies  $(U, V)$  simultaneously. To develop the more general result, we first consider a window  $w(x, y)$  as follows:

$$w(x, y) = g(x, y) * g(x, y) = \frac{1}{2\pi(\sqrt{2}\sigma_g)^2} e^{-\frac{(x^2+y^2)}{2(\sqrt{2}\sigma_g)^2}}, \quad (31)$$

where  $g(x, y)$  is the Gaussian function from (1). The window function  $w(x, y)$  is then determined entirely by parameter  $\sigma_g$ . The Fourier transform of the window function  $w(x, y)$  is:

$\mathcal{F}\{g(x, y) * g(x, y)\} = [G(u, v)]^2 = e^{-4\pi^2\sigma_g^2(u^2+v^2)}$ , where  $\mathcal{F}\{\cdot\}$  denotes the Fourier transform operator, and functions  $G(\cdot)$  and  $g(\cdot)$  are a Fourier transform pair from (1,2). We finally arrive at the desired result by taking the Fourier transform of the windowed autocorrelation  $w(x, y)R_i(x, y)$ :

$$P_i(u, v, \sigma_g) = \mathcal{F}\{w(x, y)R_i(x, y)\} = [G(u, v)]^2 * S_i(u, v), \quad (32)$$

where we add the argument  $\sigma_g$  to  $P_i(u, v)$  to explicitly indicate the dependence of  $P_i$  on this parameter. The dependence arises because the functions  $w(x, y)$  and  $G(u, v)$  depend on  $\sigma_g$ .

$P_i(u, v, \sigma_g)$  represents total output power of the Gabor prefiltered image  $i_{h_i}(x, y)$  for a Gabor prefilter with center frequency  $(u, v)$  and parameter  $\sigma_g$ . Eq. (32) can be implemented efficiently using the FFT. This discrete form of (32) then gives  $P_i(u, v)$  at a discrete set of center frequencies  $(u, v)$  and for a particular  $\sigma_g$ .

*Acknowledgements* — This work was partially supported by NIH FIRST award #CA53607 from the National Cancer Institute of the National Institutes of Health. Portions of this manuscript were presented elsewhere [21].



## REFERENCES

- [1] A. C. Bovik, M. Clark, and W. S. Geisler, "Multichannel texture analysis using localized spatial filters," *IEEE Trans. Pattern Anal. Machine Intell.*, **12**(1), 55–73 (1990).
- [2] A. C. Bovik, "Analysis of multichannel narrow-band filters for image texture segmentation," *IEEE Trans. Signal Processing*, **39**(9), 2025–2043 (1991).
- [3] A. K. Jain and F. Farrokhnia, "Unsupervised texture segmentation using Gabor filters," *Pattern Recognition*, **23**(12), 1167–1186 (1991).
- [4] A. C. Bovik, N. Gopal, T. Emmoth, and A. Restrepo, "Localized measurements of emergent image frequencies by Gabor wavelets," *IEEE Trans. Inform. Theory*, **38**(2), 691–711 (1992).
- [5] D. Dunn, W. Higgins, and J. Wakeley, "Texture segmentation using 2-D Gabor elementary functions," *IEEE Trans. Pattern Anal. and Machine Intell.*, **16**(2), 130–149 (1994).
- [6] J. Bigun and J. M. H. du Buf, "N-folded symmetries by complex moments in Gabor space and their application to unsupervised texture segmentation," *IEEE Trans. Pattern Anal. Machine Intell.*, **16**(1), 80–87 (1994).
- [7] D. F. Dunn and W. E. Higgins, "Optimal Gabor filters for texture segmentation," *IEEE Trans. Image Proc.*, **4**(7), 947–964 (1995).
- [8] T. P. Weldon, W. E. Higgins, and D. F. Dunn, "Efficient Gabor filter design for texture segmentation," to appear in *Pattern Recognition*, (1996).
- [9] T. P. Weldon, *Multiresolution Design of Multiple Gabor Filters for Texture Segmentation*. PhD thesis, The Pennsylvania State University, (1995).
- [10] T. N. Tan, "Texture edge detection by modelling visual cortical channels," *Pattern Recognition*, **28**(9), 1283–1298 (1995).
- [11] D. P. Casasent, J. S. Smokelin, and A. Ye, "Wavelet and Gabor transforms for detection," *Optical Eng.*, **31**(9), 1893–1898 (1992).
- [12] D. P. Casasent and J.-S. Smokelin, "Real, imaginary, and clutter Gabor filter fusion for detection with reduced false alarms," *Optical Eng.*, **33**(7), 2255–2263 (1994).
- [13] B. J. Super and A. C. Bovik, "Localized measurement of image fractal dimension using Gabor filters," *Journal of Visual Comm. and Image Representation*, **2**(2), 114–128 (1991).
- [14] A. K. Jain and S. Bhattacharjee, "Text segmentation using Gabor filters for automatic document processing," *Machine Vision and Applications*, **5**, 169–184 (1992).
- [15] R. Mehrotra, K. R. Namuduri, and N. Ranganathan, "Gabor filter-based edge detection," *Pattern Recognition*, **25**(12), 1479–1493 (1992).
- [16] J. G. Daugman, "High confidence visual recognition of persons by a test of statistical independence," *IEEE Trans. Pattern Anal. Machine Intell.*, **15**(11), 1148–1160 (1993).
- [17] J. G. Daugman, "Complete discrete 2-D Gabor transforms by neural networks for image analysis and compression," *IEEE Trans. Acoust., Speech, Signal Processing*, **36**(7), 1169–1179 (1988).
- [18] T. Ebrahimi and M. Kunt, "Image compression by Gabor expansion," *Optical Eng.*, **30**(7), 873–880 (1991).
- [19] M. Porat and Y. Zeevi, "The generalized Gabor scheme of image representation in biological and machine vision," *IEEE Trans. Pattern Anal. Machine Intell.*, **10**(4), 452–468 (1988).
- [20] J. G. Daugman, "Uncertainty relation for resolution in space, spatial frequency, and orientation optimized by two-dimensional visual cortical filters," *J. Opt. Soc. Amer. A*, **2**(7), 1160–1169 (1985).
- [21] T. P. Weldon and W. E. Higgins, "Multiscale Rician approach to Gabor filter design for texture segmentation," in *IEEE Int. Conf. on Image Processing*, Austin, TX, 13–16 Nov., vol. II, 620–624 (1994).
- [22] M.-T. Leung, W. E. Engler, and P. Frank, "Fingerprint image processing using neural network," in *IEEE Reg 10 Conf. on Computer and Comm. Systems*, Hong Kong, 582–586 (1990).
- [23] M. R. Turner, "Texture discrimination by Gabor functions," *Biological Cybernetics*, **55**, 71–82 (1986).
- [24] T. Randen and J. H. Husøy, "Novel approaches to multichannel filtering for image texture segmentation," in *SPIE Visual Comm. Image Proc. 1994*, vol. 2094, 626–636 (1994).
- [25] J. Malik and P. Perona, "Preattentive texture discrimination with early vision mechanisms," *J. Opt. Soc. Amer. A*, **7**(5), 923–932 (1990).
- [26] J. M. H. du Buf, "Abstract processes in texture discrimination," *Spatial Vision*, **6**, 221–242 (1992).
- [27] T. Chang and C. C. J. Kuo, "Texture analysis and classification with tree-structured wavelet transform," *IEEE Trans. Image Proc.*, **2**(4), 429–441 (1993).
- [28] R. O. Duda and P. E. Hart, *Pattern Classification and Scene Analysis*, John Wiley and Sons (1973).
- [29] T. Weldon and W. Higgins, "Design of multiple Gabor filters for texture segmentation," to appear in *IEEE Int. Conf. Acous., Speech, Sig. Proc.*, Atlanta, GA, 7–10 May, (1996).
- [30] T. P. Weldon and W. E. Higgins, "Integrated approach to texture segmentation using multiple Gabor filters," to appear *IEEE Int. Conf. on Image Processing*, Lausanne Switzerland, 16–19 Sept., (1996).
- [31] T. P. Weldon, W. E. Higgins, and D. F. Dunn, "Efficient Gabor filter design using Rician output statistics," in *IEEE Int. Symp. Circuits, Systems*, London, England, 30 May –2 June, vol. 3, 25–28 (1994).
- [32] D. F. Dunn and W. E. Higgins, "Optimal Gabor-filter design for texture segmentation," in *Proc. IEEE Int. Conf. Acoust., Speech, Signal Processing*, vol. V, V37–V40 (1993).
- [33] M. Schwartz, *Information Transmission, Modulation, and Noise*, third ed., McGraw-Hill, New York, NY (1980).
- [34] S. Rice, "Mathematical analysis of random noise," *Bell System Tech. Journal*, **23**, 282–333 (1944).
- [35] S. Rice, "Mathematical analysis of random noise," *Bell System Tech. Journal*, **24**, 96–157 (1945).
- [36] A. Papoulis, *Probability, Random Variables, and Stochastic Processes*, second ed., McGraw-Hill, New York, NY (1984).
- [37] R. C. Gonzalez and R. E. Woods, *Digital Image Processing*, Addison-Wesley, New York, NY (1992).
- [38] P. Brodatz, *Textures: A Photographic Album for Artists and Designers*, Dover, New York, NY (1966).
- [39] D. F. Dunn, T. P. Weldon, and W. E. Higgins, "Extracting halftones from printed documents using texture analysis," to appear *IEEE Int. Conf. on Image Processing*, Lausanne, Switzerland, 16–19 Sept., (1996).

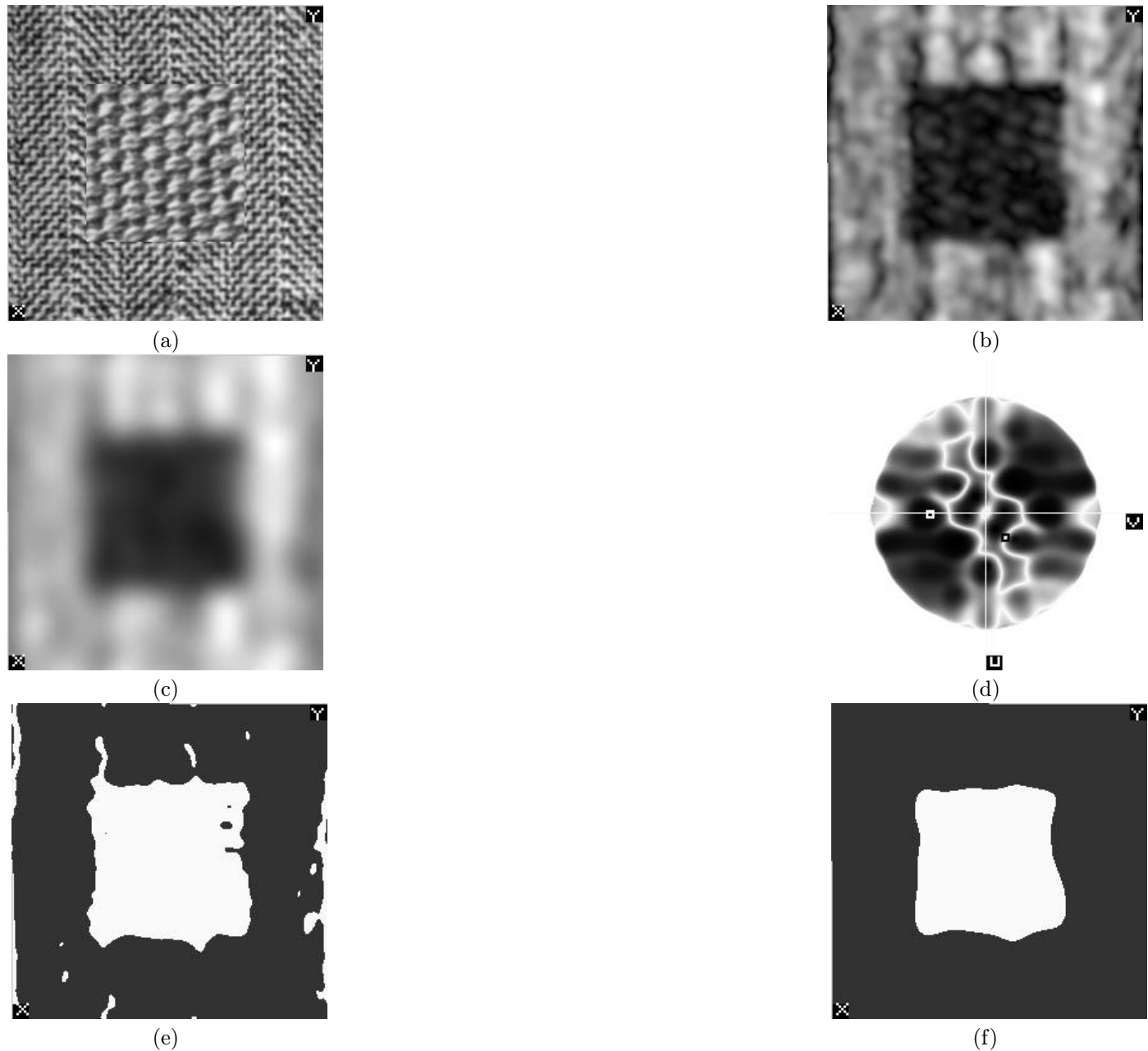


Fig. 3. Results for optimal filter center frequency  $(U, V) = (.004, -.176)$ : (a) Input composite image: outer border is d16 "herringbone weave," interior square is d77 "cotton canvas." (b) Prefilter output  $m(x, y)$ ,  $\sigma_g = 5$ . (c) Postfiltered output  $m_p(x, y)$ ,  $\sigma_p = 10$ . (d) Segmentation error versus  $(U, V)$ , white=100%, black=0%;  $(U, V) = (0, 0)$  at center of image. The white box indicates the center frequency of the prefilter design. (e) Segmentation of prefiltered output. (f) Segmentation of postfiltered output.

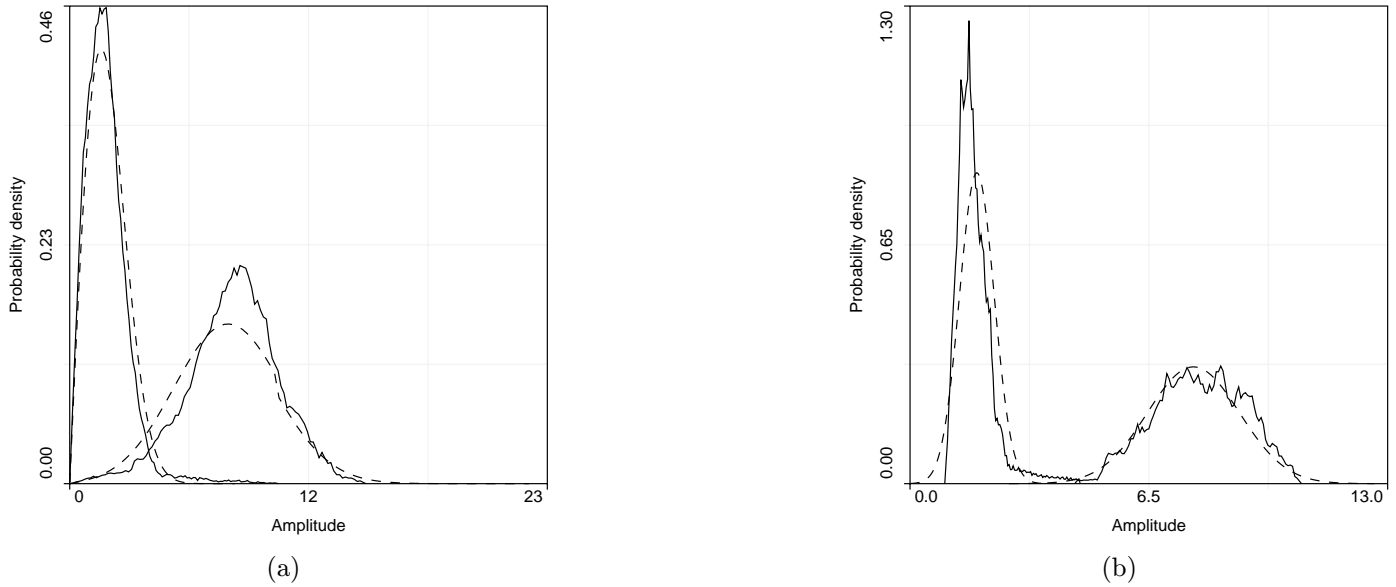


Fig. 4. Histograms of filtered images in Fig. 3: (a) Predicted (dashed) and actual (solid) histograms of  $m(x, y)$ . (b) Predicted (dashed) and actual (solid) histograms of  $m_p(x, y)$ . The histograms that peak at the lower amplitude in (a) and (b) correspond to the darker regions in the images of  $m(x, y)$  and  $m_p(x, y)$  in Fig. 3.

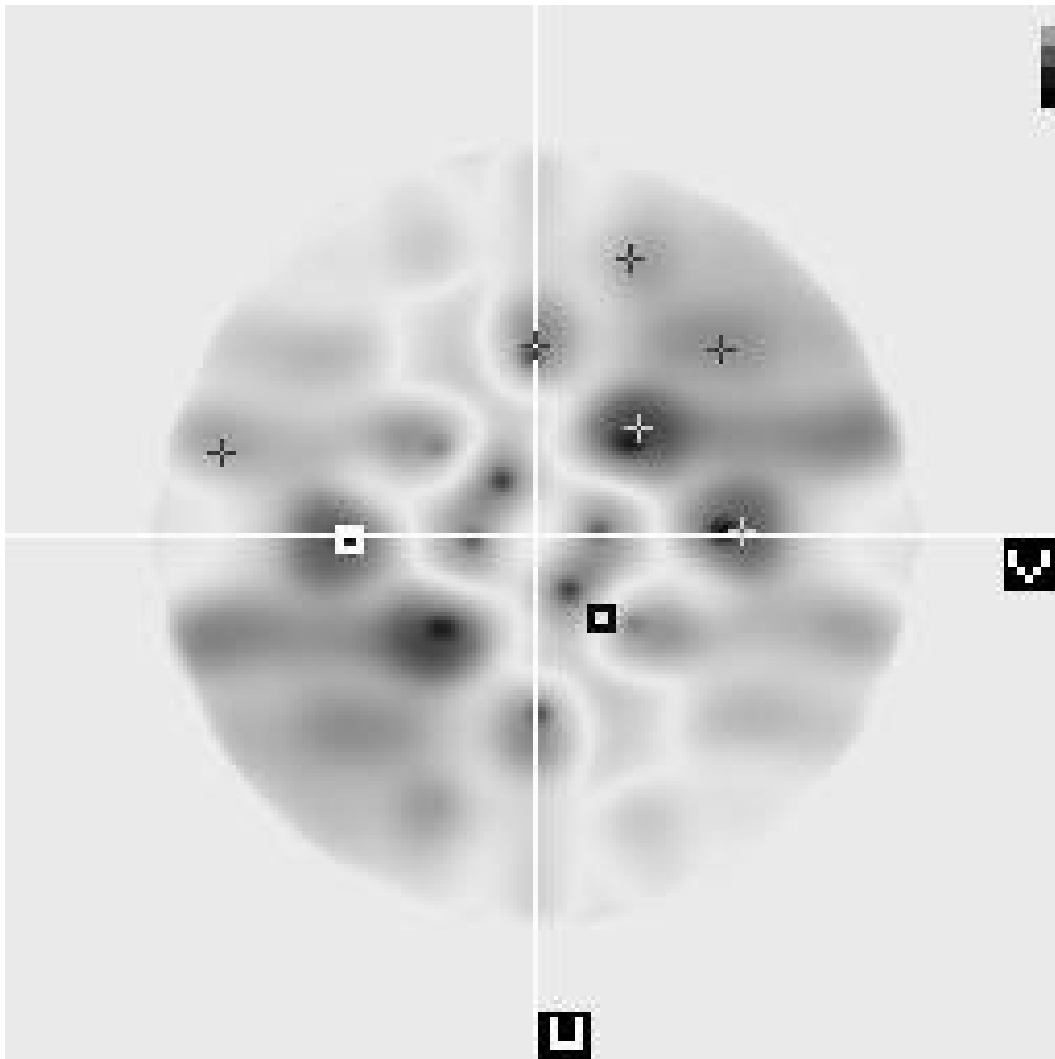


Fig. 5. Predicted error for the example of Fig. 3, d16 “herringbone weave” (border) d77 “cotton canvas” (center). The intensity is logarithmically proportional to error, the center corresponds to  $(u, v) = (0, 0)$ , and the lower right corner corresponds to positive  $u$  and  $v$ . The white box surrounds the Gabor-filter center frequency selected by the proposed filter-design algorithm. The +’s correspond to frequencies selected by the Dunn and Higgins algorithm. [7]

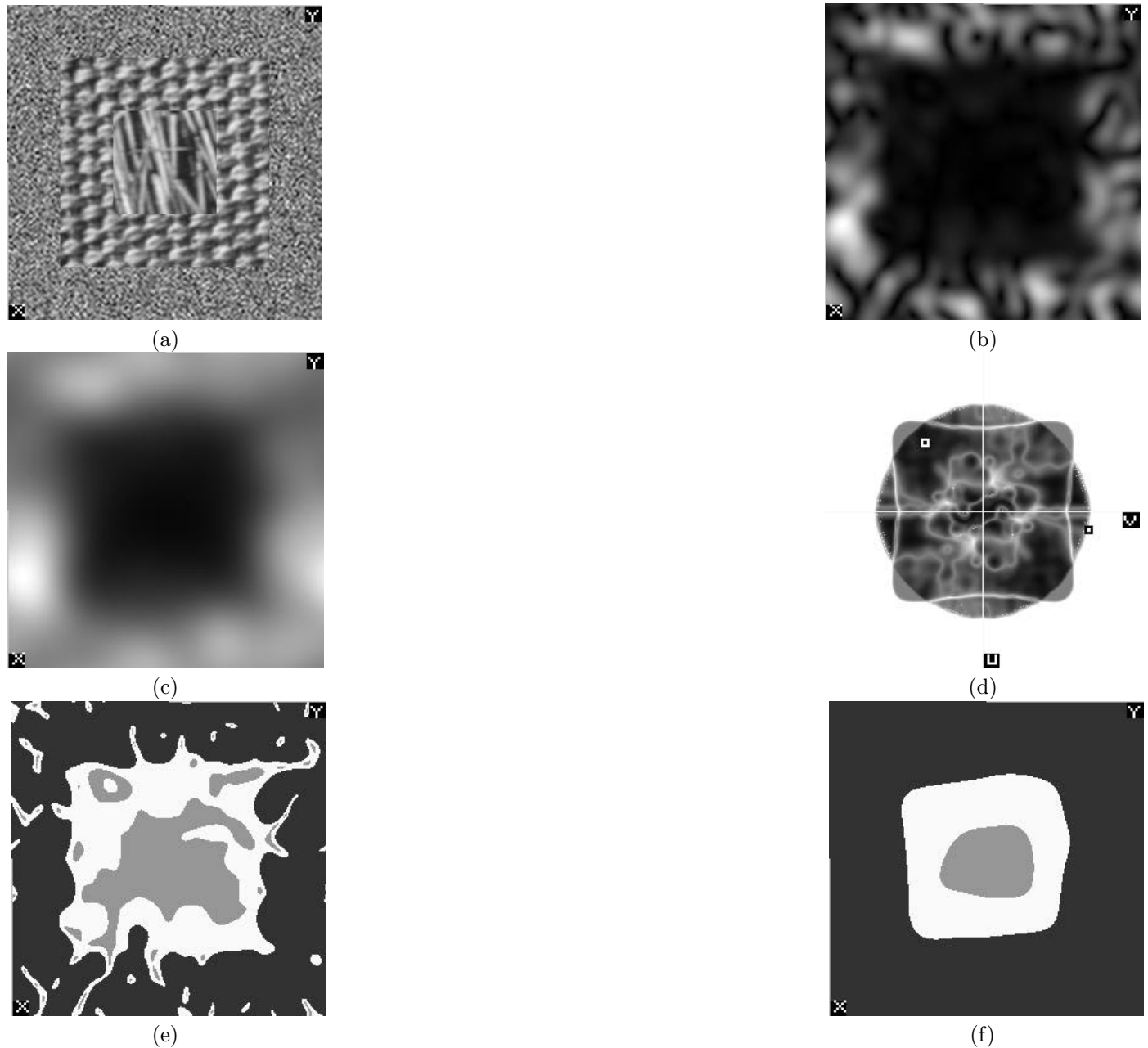


Fig. 6. Results for optimal filter, center frequency  $(U, V) = (-.219, -.184)$ : (a) Input composite image: outer border is lowpass uniform noise, middle ring is d15 “cotton canvas”, interior square is d77 “straw.” (b) Prefilter output  $m(x, y)$ ,  $\sigma_g = 9$ . (c) Postfiltered output  $m_p(x, y)$ ,  $\sigma_p = 18$ . (d) Segmentation error versus  $(U, V)$ , white=100%, black=0%;  $(u, v) = (0, 0)$  at center of image. The white box indicates the center frequency of the prefilter design. (e) Segmentation of prefiltered output. (f) Segmentation of postfiltered output.

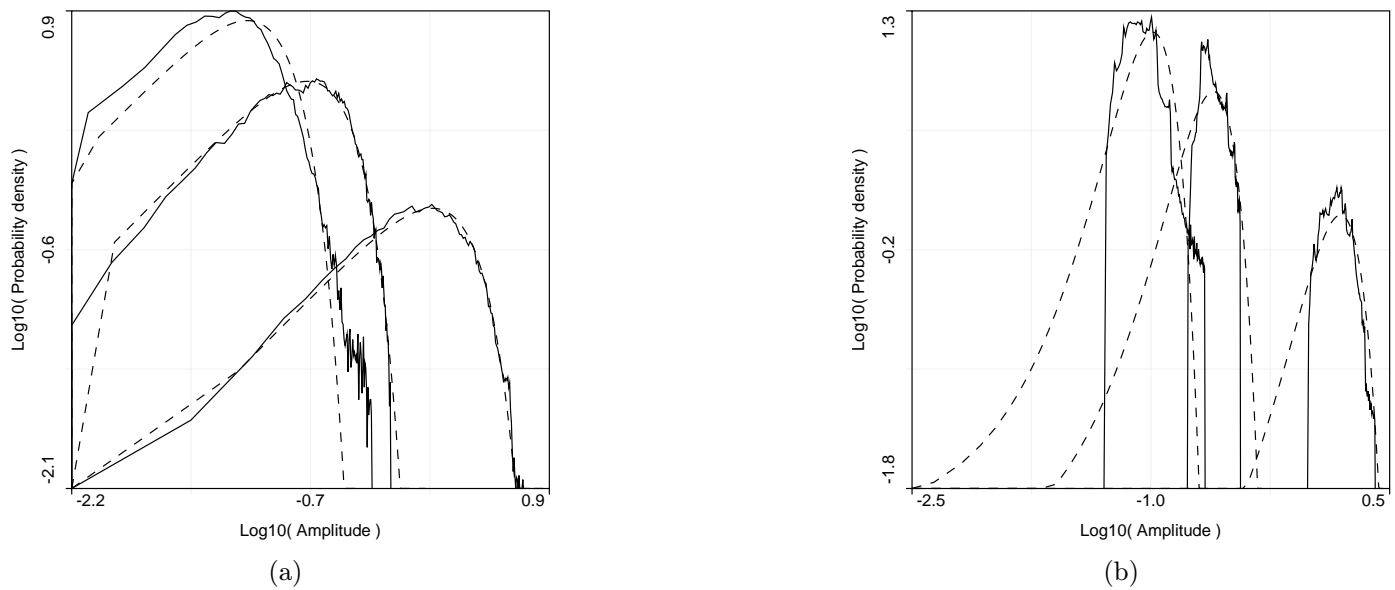


Fig. 7. Histograms of filtered images in Fig. 6: (a) Predicted (dashed) and actual (solid) histograms of  $m(x, y)$ . (b) Predicted (dashed) and actual (solid) histograms of  $m_p(x, y)$ . The histograms that peak at the lowest amplitude in (a) and (b) correspond to the darkest regions (d77) in the images of  $m(x, y)$  and  $m_p(x, y)$  in Fig. 6; the histograms peaking at the largest amplitude correspond to the brightest region (noise).

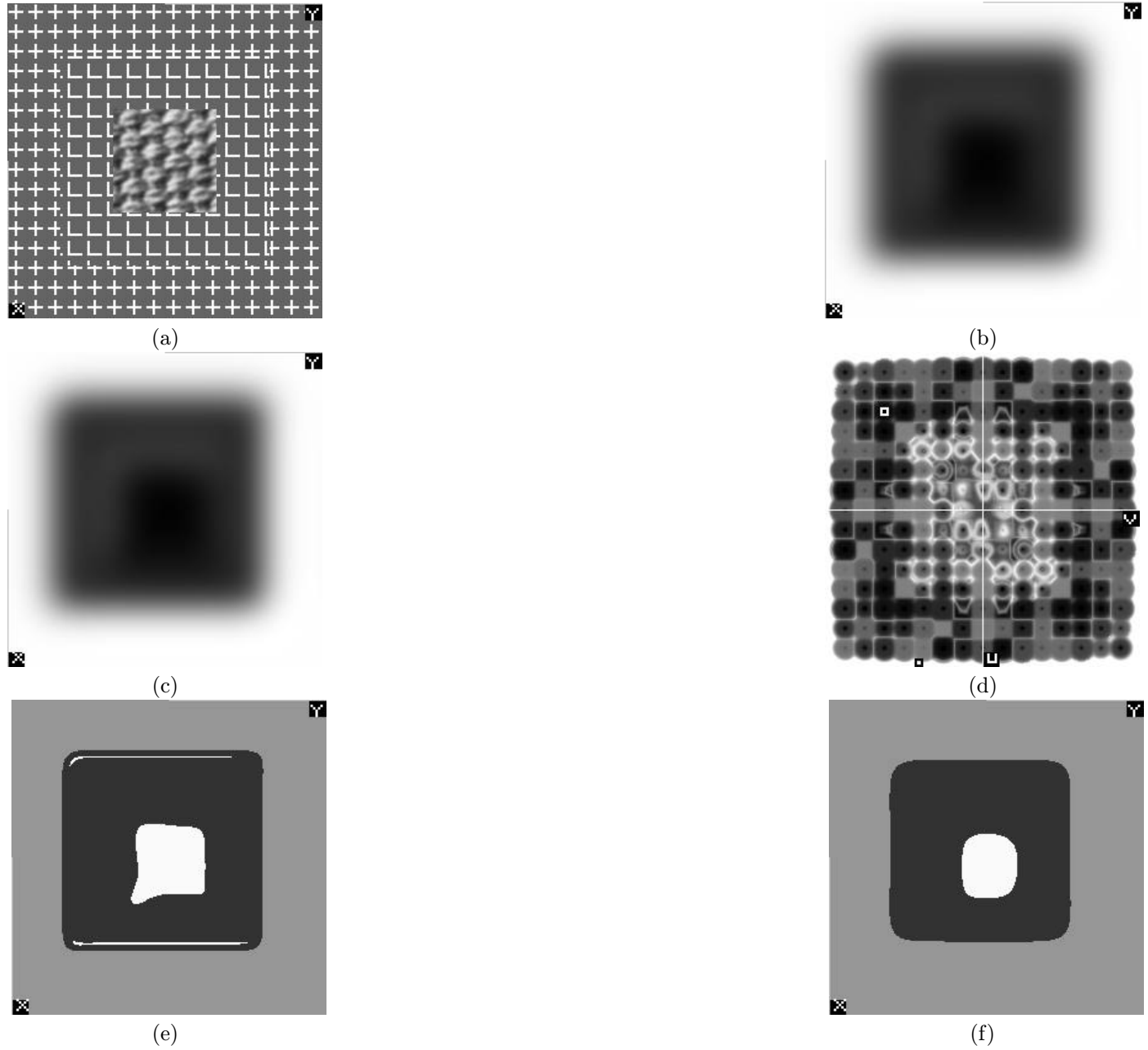


Fig. 8. Results for optimal filter center frequency  $(U, V) = (-.312, -.312)$ : (a) Input composite image: outer border is “+,” middle ring is “L,” interior square is d77 “cotton canvas.” (b) Prefilter output  $m(x, y)$ ,  $\sigma_g = 9$ . (c) Postfiltered output  $m_p(x, y)$ ,  $\sigma_p = 12.6$ . (d) Segmentation error versus  $(U, V)$ , white=100%, black=0%;  $(U, V) = (0, 0)$  at center of image. The white box indicates the center frequency of the prefilter design. (e) Segmentation of prefiltered output. (f) Segmentation of postfiltered output.

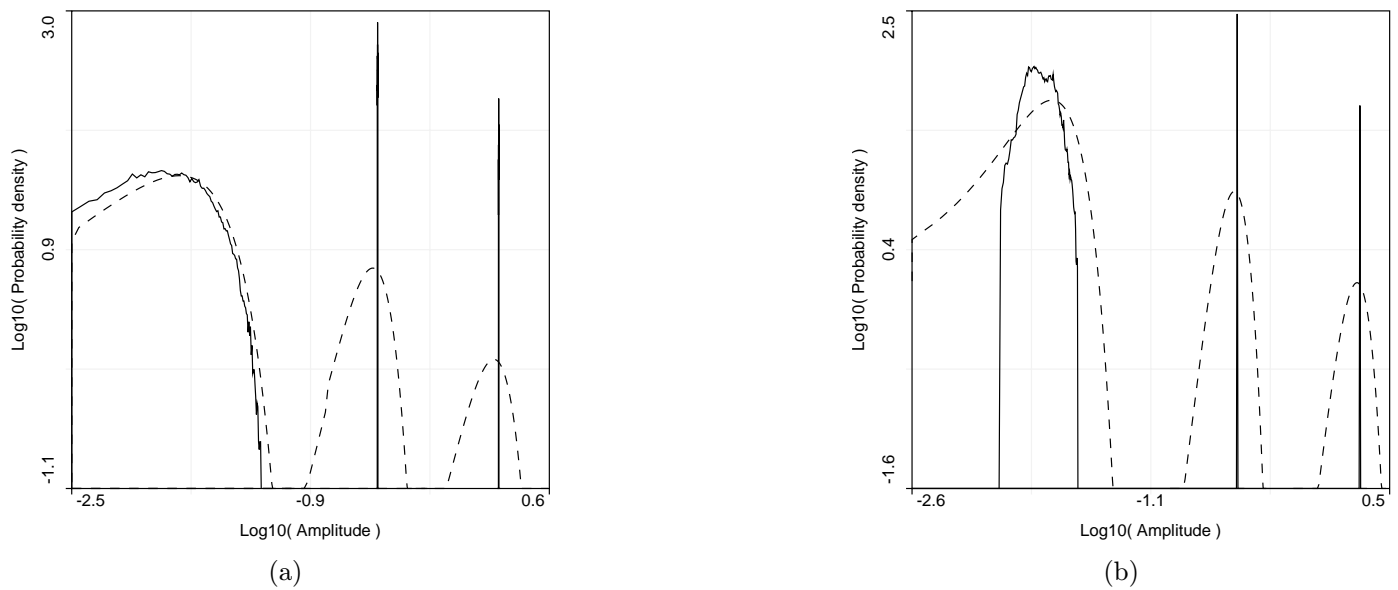


Fig. 9. Histograms of filtered images in Fig. 8: (a) Predicted (dashed) and actual (solid) histograms of  $p m(x, y)$ . (b) Predicted (dashed) and actual (solid) histograms of  $m_p(x, y)$ . The histograms that peak at the lowest amplitude in (a) and (b) correspond to the darkest regions (d77) in the images of  $m(x, y)$  and  $m_p(x, y)$  in Fig. 8; the histograms peaking at the largest amplitude correspond to the brightest region (“+”).



Thomas Weldon received the B.S., M.Eng., and Ph.D. in electrical engineering from Penn State in 1979, 1989, and 1995. From 1979 to 1982 he designed portable communications equipment at Motorola in Plantation, Florida. From 1982 to 1984 he designed microelectronic circuits at Alpha Industries in Lansdale, Pennsylvania. From 1984 to 1990 he developed signal processing and microwave communication systems as a senior engineer at American Electronic Laboratories in Lansdale, Pennsylvania. From 1990 to 1995 he was engaged in signal-processing and image-processing research at Penn State while completing his Ph.D. In 1995 he joined the University of North Carolina at Charlotte as

an assistant professor of electrical engineering, where he is presently engaged in research on image processing and biotelemetry systems. His current research interests are image processing, signal processing, biomedical imaging, biotelemetry, and communication systems. He is a member of the SPIE, IEEE, and the Pattern Recognition Society.

William E. Higgins obtained the B.S. degree in electrical engineering (1979) at the Massachusetts Institute of Technology and the M.S. (1981) and Ph.D. (1984) degrees in electrical engineering at the University of Illinois, Urbana. Previously, he worked as a principal research scientist at the Honeywell Systems and Research Center (1984-1987), Minneapolis, MN, working in the field of automatic target-recognition systems. He later was a senior research fellow in the Biodynamics Research Unit of the Mayo Clinic (1987-1989), Rochester, MN, working in the areas of multidimensional image analysis and visualization. Since 1989, he has been at the Pennsylvania State University, University Park, PA, where he is currently an associate professor in the departments of electrical engineering, computer science and engineering, and bioengineering. His research interests are in image processing, computer vision, scientific visualization, and medical image analysis. He is a member of the SPIE, IEEE, ACM, Sigma Xi, Tau Beta Pi, Eta Kappa Nu, and the Pattern Recognition Society.

Dennis Dunn received the B.S. degree in chemical engineering from Case Western Reserve University in 1969, the M.Eng. degree in engineering science from The Pennsylvania State University in 1981, and the Ph.D. degree in computer science from the Pennsylvania State University in 1992. He is presently an Assistant Professor with the Computer Science and Engineering Department, The Pennsylvania State University. His main research interests are computer vision, image processing, texture analysis, interpreting cursive text, and human-vision modeling.